ELSEVIER

Volume 186, February 2012

CONTENTS

JOURNAL OF SOLID STATE CHEMISTRY

www.elsevier.com/locate/jssc

Abstracted/indexed in BioEngineering Abstracts, Chemical Abstracts, Coal Abstracts, Current Contents/Physics, Chemical, & Earth Sciences, Engineering Index, Research Alert, SCISEARCH, Science Abstracts, and Science Citation Index. Also covered in the abstract and citation database SciVerse SCOPUS®. Full text available on SciVerse ScienceDirect®.

Regular Articles

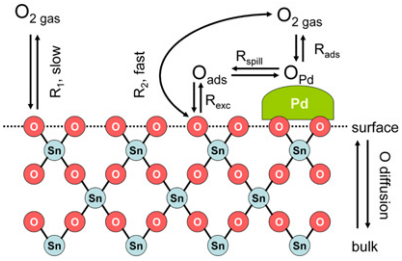

Nanocrystalline SnO_2 modification by Pd essentially influences the interaction with gas phase molecules. A temperature programmed isotopic exchange study revealed that Pd promotes oxygen exchange of the material by facilitating oxygen dissociation and spill-over on the surface of active clusters.

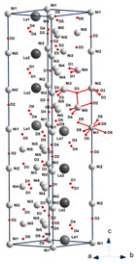

The detailed D atoms arrangement in $La_{1.63}Mg_{0.37}Ni_7D_{8.8}$ differs significantly from the previously reported $La_{1.5}Mg_{0.5}Ni_7D_{8.9(9.1)}$. The present model consists of only five deuterium sites as opposed to nine proposed for $La_{1.5}Mg_{0.5}Ni_7D_{8.9(9.1)}$. The reported four remaining deuterium atom positions in $La_{1.5}Mg_{0.5}Ni_7D_{8.9(9.1)}$ were not found in the investigated $La_{1.63}Mg_{0.37}Ni_7D_{8.8}$. The five Ni atoms have deuterium among their nearest neighbors, which surround them in a way similar to configurations observed in some complex transition metal hydrides and already reported for metallic hydrides. In the presented deuterium-rich phase, deformed tetrahedron, rigid trigonal pyramids as well as disordered and deformed saddle-like configuration are observed.

Regular Articles—Continued

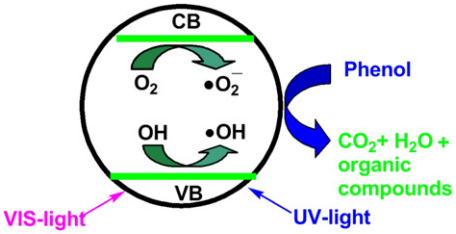

The photocatalytic reaction initiated by the photoexcitation of the semiconductor (ZnO), leads to the formation of electron–hole, while part of the electron–hole pairs recombine, some holes combine with water to form •OH radicals and some electrons convert oxygen to super oxide radical ($\bullet O_2^-$).

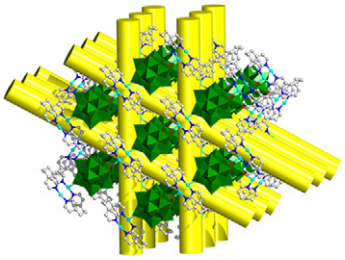

An unusual example of mono-substituted Keggin anion-chain based hybrid compound that possesses a 3D structure has been synthesized, which offers a feasible route for synthesis of such compounds.

Continued

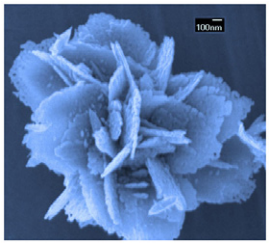

Nanosheets-based corundum In_2O_3 microflowers were fabricated by one-pot hydrothermal treatment of D-fructose/$In(NO_3)_3$ mixture followed by calcination, which show high performance for formaldehyde sensing.

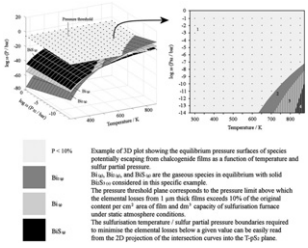

Example of 3D plot showing the equilibrium pressure surfaces of species potentially escaping from chalcogenide films as a function of temperature and sulfur partial pressure.

$Bi_{(g)}$, $Bi_{2(g)}$, and $BiS_{(g)}$ are the gaseous species in equilibrium with solid $Bi_2S_{3(s)}$ considered in this specific example.

The pressure threshold plane corresponds to the pressure limit above which the elemental losses from 1 μm thick films exceeds 10% of the original content per cm^2 area of film and dm^3 capacity of sulfurization furnace under static atmosphere conditions.

The sulfurization temperature/sulfur partial pressure boundaries required to minimise the elemental losses below a given value can be easily read from the 2D projection of the intersection curves into the T-p_{S2} plane.

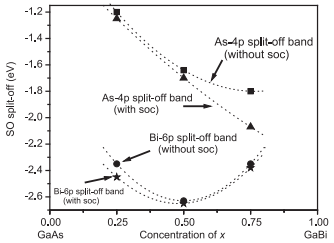

Bowing effect of spin–orbit split-off band values versus Bi content with and without spin–orbit coupling for $GaAs_{1-x}Bi_x$ (at $x = 0.25$, 0.50 and 0.75). Calculations are done with GGA.

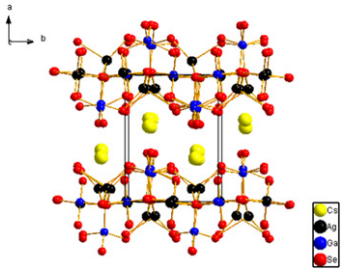

$CsAgGa_2Se_4$ contains two-dimensional $^2_\infty[AgGa_2Se_4]^-$ layers with a novel chain–sublayer–chain structure.

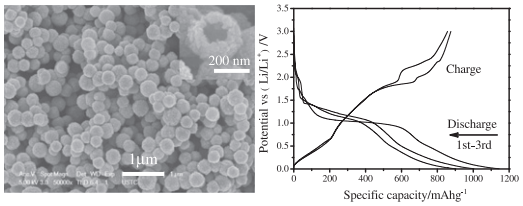

$CuInS_2$ hollow nanospheres was successfully prepared from Cu_2O solid nanospheres in the absence of any surfactant, which can deliver a large initial discharge capacity of 1144 mAh g^{-1} and exhibit good cycle performance.

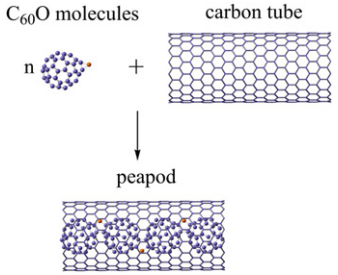

Formation of the novel peapod—1D $C_{60}O$ polymer encapsulated inside single-walled carbon nanotube.

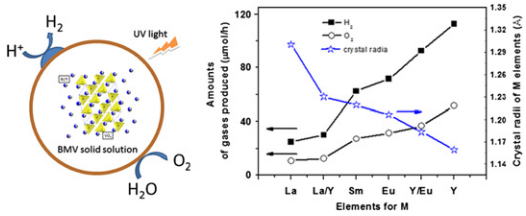

Novel $Bi_{0.5}M_{0.5}VO_4$ (*M* = La, Eu, Sm and Y) solid solutions showed the high and stable photocatalytic activities for overall water splitting with their crystal radii of *M* elements.

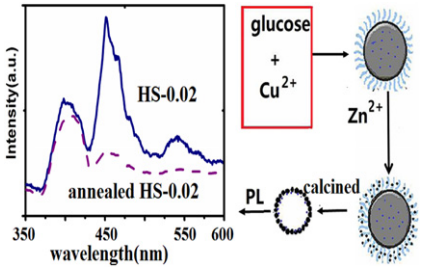

CuO–ZnO hollow spheres were obtained using Cu-embedded carbon spheres as template, and the photoluminescent spectra afforded the evidence regarding the oxygen vacancies in the hollow spheres.

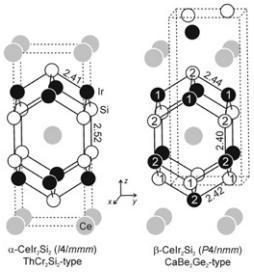

The crystal structures of α- and β-$CeIr_2Si_2$. Relevant interatomic distances (Å), the three-dimensional $[Ir_2Si_2]$ networks and the crystallographically independent iridium and silicon sites are indicated.

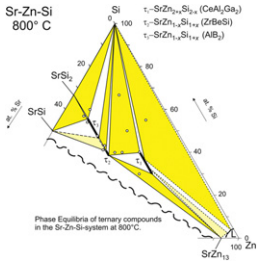

Phase equilibria of ternary compounds in the Sr–Zn–Si-system at 800 °C.

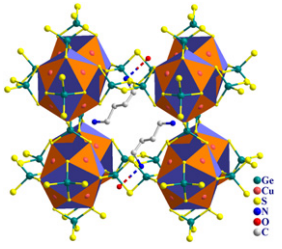

Compound **1** contains a 3D expanded framework constructed from icosahedral Cu_8S_{12} clusters linked by GeS_4 and dimeric Ge_2S_6 units, with diprotonated 1,4-dab and H_2O molecules located in the channels.

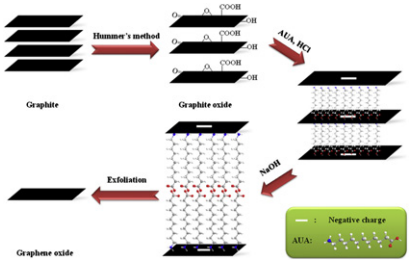

A stable graphene oxide suspension could be quickly prepared by exfoliating a graphite oxide suspension by a host–guest electrostatic repulsion in aqueous solution.

Continued

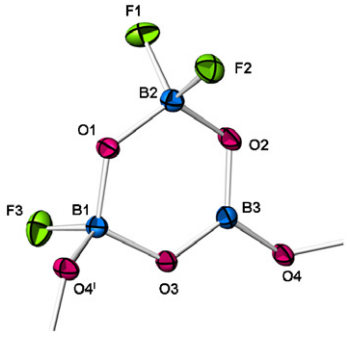

Repetition unit of $Li_2B_3O_4F_3$.

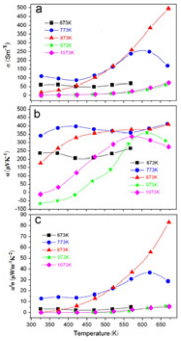

The samples sintered above 873 K, both of the Seebeck coefficient and electrical conductivity exhibit an increase tendency with increasing temperature, which is due to the mechanism of mix-conduction for $CuCrS_2$.

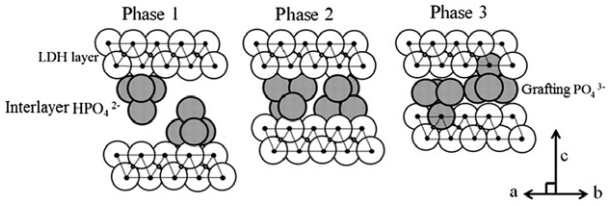

The cross section of the synthetic Mg, Al layered double hydroxides in Phase 1, with interlayer hydrogen phosphate Phase 2, and with grafted phosphate, Phase 3.

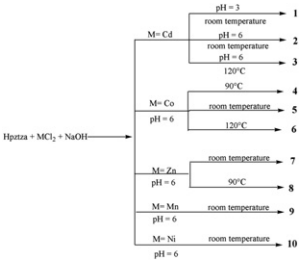

Ten new coordination polymers with 2-(5-(pyrazin-2-yl)-2H-tetrazol-2-yl) acetic acid (Hpztza) ligand have been synthesized and their structures have been characterized. All of the complexes show photoluminescence at room temperature.

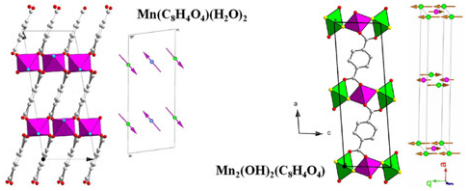

The macroscopic magnetic properties and magnetic structures of two metal-organic frameworks based on manganese (II) and terephthalate molecules are presented.

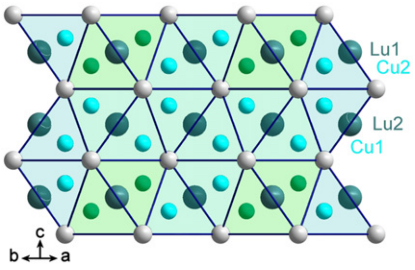

In the series of the $\sim RCu_3S_3$ and $\sim RCuTe_2$ compounds the R and Cu atoms occupy disordered positions. The S(Te) atoms are stacked in a close packed arrangement with the layers in the sequence *AB*.

A novel approach for enhanced visible light activity in doped nanosize titanium dioxide through the excitons trapping
Kanakkanmavudi B. Jaimy, K.V. Baiju, Swapankumar Ghosh and K.G.K. Warrier
page 149

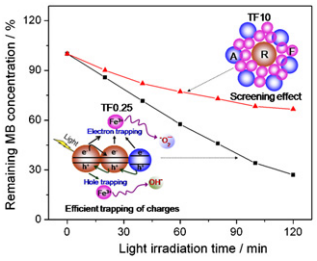

Model explaining the transfer and trapping of e^-/h^+ pairs in mixed phase titania by Fe^{3+} ions suggests the reason for the increased lifetime of e^-/h^+ pairs and enhanced photocatalytic activity.

Synthesis and characterization of uranyl chromate sheet compounds containing edge-sharing dimers of uranyl pentagonal bipyramids
Daniel K. Unruh, Michelle Baranay, Laura Pressprich, Megan Stoffer and Peter C. Burns
page 158

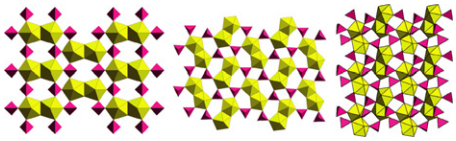

Eight uranyl chromate compounds containing sheet structural units built from uranyl pentagonal bipyramids and $(CrO_4)^{2-}$ tetrahedra are reported. Relationships between sheet topologies and interstitial constituents is examined.

Hydrothermal synthesis, crystal structures and photoluminescence properties of mixed europium–yttrium organic frameworks
Yinfeng Han, Lianshe Fu, Luís Mafra and Fa-Nian Shi
page 165

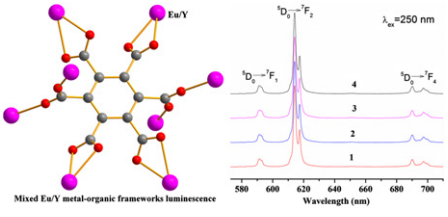

Three mixed europium and yttrium organic frameworks: $Eu_{2-x}Y_x(Mel)(H_2O)_6$ (Mel = mellitic acid) have been synthesized and characterized. All the compounds contain a 3-D net with (4, 8)-flu topology. The study indicates that the photoluminescence properties are effectively affected by the different ratios of europium and yttrium ions, the quantum efficiency is increased and the Eu^{3+} lifetime becomes longer in these MOFs than those of the Eu analog.

Spectroscopic studies of sulfite-based polyoxometalates at high temperature and high pressure
Raul Quesada Cabrera, Steven Firth, Christopher S. Blackman, De-Liang Long, Leroy Cronin and Paul F. McMillan
page 171

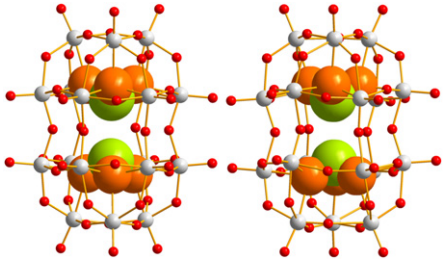

Structural changes occurring within non-conventional Dawson-type $[\alpha/\beta\text{-}Mo_{18}O_{54}(SO_3)_2]^{4-}$ polyanions in the form of tetrapentylammonium salts were studied by a combination of IR, Raman and visible spectroscopy at high temperature and high pressure. Evidence of the formation of bronze-type materials above 400 K and also upon pressurization to 8 GPa is presented. This conclusion is suggested to be a general result for polyoxometalate compounds subjected to extreme conditions and it opens opportunities for the design of new materials with interesting optical and electronic properties.

Syntheses and crystal structures of the quaternary uranium lanthanide oxyselenides $UYb_2O_2Se_3$ and $U_2Ln_2O_4Se_3$ (Ln = Pr, Sm, Gd)
Adam D. Raw and James A. Ibers
page 177

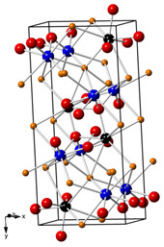

The $U_2Ln_2O_4Se_3$ (Ln = Pr, Sm, Gd) structure: primarily U sites are in black, primarily Ln sites are in blue, O red, Se orange.

Sn-doped polyhedral In_2O_3 particles: Synthesis, characterization, and origins of luminous emission in wide visible range
Yunqing Zhu and Yiqing Chen
page 182

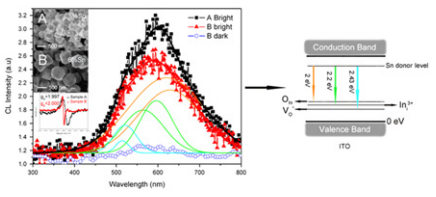

With more oxygen vacancies and tin doping. ITO particles can exhibit a better CL performance. Sn donor level near the conduction band edge plays an important role in luminous emission in wide visible range.

Continued

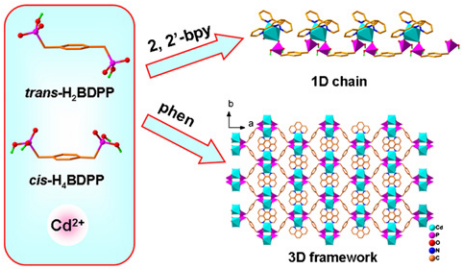

Two new cadmium diphosphonates were obtained by using two different auxiliary ligands. The influence of the N-donor ligands on the structure of the complexes is discussed.

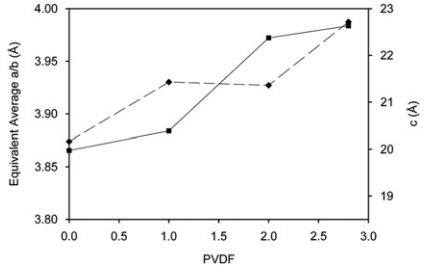

Low temperature (375 °C) fluorination of $Sr_3Fe_2O_{7-x}$ with poly(vinylidene fluoride) leads to the production of three new Ruddlesden Popper oxide fluorides with progressive filling of the anion sites within the structure.

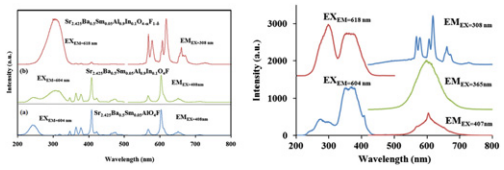

After the replacement of Sr^{2+} and Al^{3+} ions by Sm^{3+} and In^{3+} ions in $Sr_{2.5}Ba_{0.5}AlO_4F$ host structure, a novel charge-transfer band centered around 304 nm shifted from 240 nm is monitored; moreover, sharp and well-resolved emission peaks in the $^4G_{5/2} \rightarrow {}^6H_J$ transitions of the Sm^{3+} activator are observed (Figure, Left). The diverse excitation and emission photoluminescence spectra of $Sr_{2.5-3x/2}Ba_{0.5}Sm_xAl_{1-y}In_yO_{4-\alpha}F_{1-\delta}$ ($0.001 \le x$, $y \le 0.1$) phosphors originated by the charge-transfer of the host to the Sm^{3+} activator, the *f*–*f* transitions in the Sm^{3+} ions, and the defect-induced self-activation are also introduced (Figure, Right).

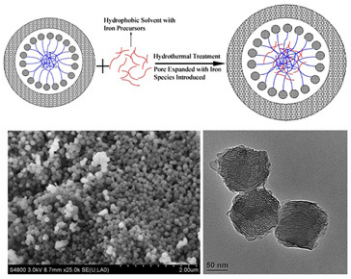

Uniform MSNs with iron active centers and large pore size have been prepared by a newly developed strategy, which demonstrates enhanced catalytic performance for benzylation of benzene by benzyl chloride.

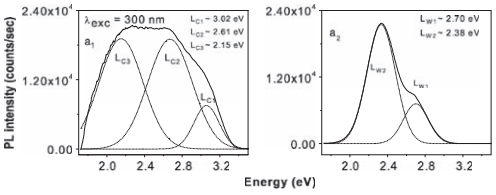

Photoluminescence spectra of ZnS with cubic (a_1) and wurtzite (a_2) structure.

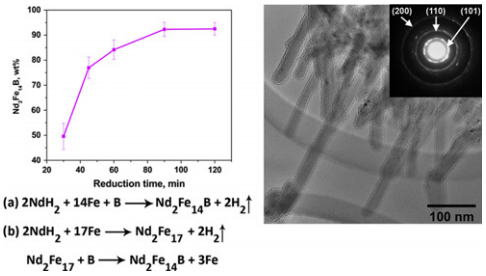

The kinetics, reaction mechanism and morphology of $Nd_2Fe_{14}B$ magnetic nanoparticles synthesized by sol–gel followed by reduction–diffusion at 800 °C.

Structural phase transitions of SrF_2 at high pressure
J.S. Wang, C.L. Ma, D. Zhou, Y.S. Xu, M.Z. Zhang, W. Gao, H.Y. Zhu and Q.L. Cui
page 231

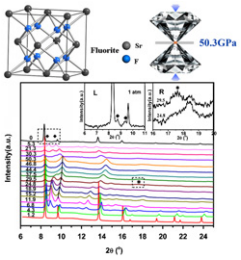

The high-pressure behavior of SrF_2 has been investigated by angle-dispersive synchrotron X-ray powder diffraction measurement up to 50.3 GPa at room temperature.

Controllable synthesis of a novel hedgehog-like core/shell structure
Shumin Wang, Hongwei Tian, Yanhui Pei, Qingnan Meng, Jianli Chen, Huan Wang, Yi Zeng, Weitao Zheng and Yichun Liu
page 235

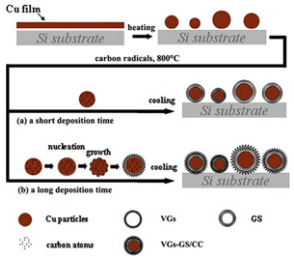

With increasing deposition time, graphene sheets extend from the surface of GS/CC, causing the multilayer graphene encapsulated copper to be converted into vertically aligned graphene sheets–graphene shell/copper core structure.

Structural and physical properties of Re substituted *B*-site ordered and disordered $SrCo_{1-x}Re_xO_{3-\delta}$ ($x = 0.1, 0.25, 0.5$)
A. Baszczuk, B. Dabrowski, S. Kolesnik, O. Chmaissem and M. Avdeev
page 240

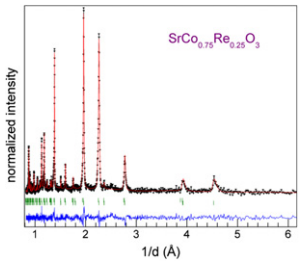

Neutron diffraction pattern for $SrCo_{0.75}Re_{0.25}O_3$. $SrCo_{0.75}Re_{0.25}O_3$ is not a partially cation ordered $Sr_4Co_3ReO_{12}$ phase, but a mixture of two structural and magnetic phases with disordered $SrCo_{1-xd}Re_{xd}O_3$ and ordered $SrCo_{1-xo}Re_{xo}O_3$ compositions where $xd > 0.1$ and $xo < 0.5$.

Microwave-assisted hydrothermal synthesis of marigold-like $ZnIn_2S_4$ microspheres and their visible light photocatalytic activity
Zhixin Chen, Danzhen Li, Guangcan Xiao, Yunhui He and Yi-Jun Xu
page 247

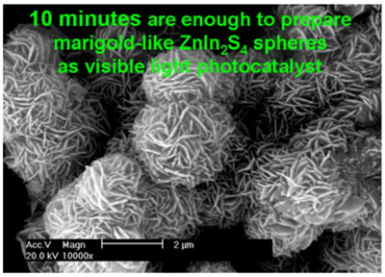

Marigold-like $ZnIn_2S_4$ microspheres were synthesized by a fast microwave-assisted hydrothermal method at 80–195 °C with a very short reaction time of 10 min. The as-prepared $ZnIn_2S_4$ sample can be used as visible light photocatalyst for degradation of organic dyes.

Large-scale controllable synthesis of dumbbell-like $BiVO_4$ photocatalysts with enhanced visible-light photocatalytic activity
Yang Lu, Yong-Song Luo, De-Zhi Kong, De-Yang Zhang, Yong-Lei Jia and Xin-Wei Zhang
page 255

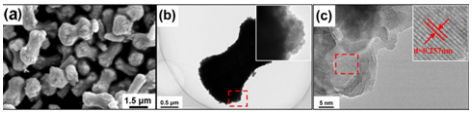

The controllable synthesis of novel dumbbell-like $BiVO_4$ hierarchical nanostructures has been successfully obtained via a simple hydrothermal route; the as-prepared $BiVO_4$ hierarchical nanostructures demonstrated the superior visible-light-driven photocatalytic efficiency.

Synthesis and characterization of CuO nanofibers, and investigation for its suitability as blocking layer in ZnO NPs based dye sensitized solar cell and as photocatalyst in organic dye degradation
R. Sahay, J. Sundaramurthy, P. Suresh Kumar, V. Thavasi, S.G. Mhaisalkar and S. Ramakrishna
page 261

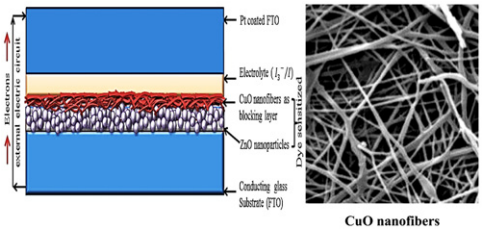

The study on the suitability of highly crystalline CuO nanofibers as the blocking layer in ZnO based DSSC was demonstrated and fabricated with possible energy applications.

Continued

Growth conditions, structure, Raman characterization and optical properties of Sm-doped $(Lu_xGd_{1-x})_2SiO_5$ single crystals grown by the Czochralski method
Michał Głowacki, Grażyna Dominiak-Dzik, Witold Ryba-Romanowski, Radosław Lisiecki, Adam Strzęp, Tomasz Runka, Mirosław Drozdowski, Viktor Domukhovski, Ryszard Diduszko and Marek Berkowski
page 268

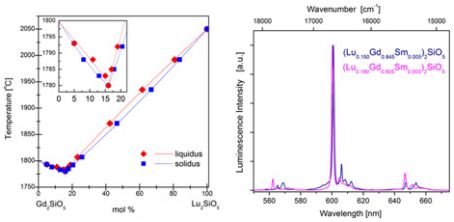

Single crystals of Sm^{3+}-doped $(Lu_xGd_{1-x})_2SiO_5$ solid solutions have been grown by Czochralski method and characterized by various techniques. Crystal structure changes from $C2/c$ to $P2_1/c$ for composition with $0.15<x<0.17$. Change of crystal structure causes changes in emission spectra.

Rapid Communication

Origin of room temperature d^0 ferromagnetism and characteristic photoluminescence in pristine SnO_2 nanowires: A correlation
Gobinda Gopal Khan, S. Ghosh and Kalyan Mandal
page 278

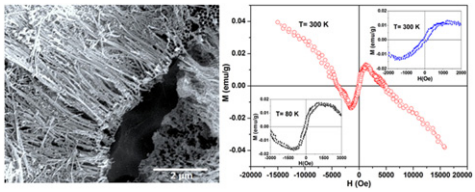

For a full and complete Guide for Authors, please go to: http://www.elsevier.com/locate/jssc

Journal of Solid State Chemistry has no page charges.